Crystal structure and superconducting properties of two-dimensional metal borocarbides XB_6C_6 (X = Al, Ga, In)

Jinni Yang,[1] Wenyuan Jin,[2] Chen Chen,[3] Jiafei Pang,[4] Xiaoyu Kuang,[1,*] Andreas Hermann,[5,†] and Cheng Lu[3,‡]

[1]*Institute of Atomic and Molecular Physics, Sichuan University, Chengdu 610065, China*

[2]*Institute of Physics, Henan Academy of Sciences, Zhengzhou 450046, China*

[3]*School of Mathematics and Physics, China University of Geosciences (Wuhan), Wuhan 430074, China*

[4]*College of Physics, Chengdu University of Technology, Chengdu 610059, China*

[5]*Centre for Science at Extreme Conditions and School of Physics and Astronomy, The University of Edinburgh, Edinburgh EH9 3FD, United Kingdom*

(Received 12 May 2026; revised 21 September 2026; accepted 16 October 2026; published 3 November 2026)

Two-dimensional (2D) metal borocarbide superconductors represent an emerging category of low-dimensional materials consisting of boron, carbon, and metal atoms, which hold substantial promise for applications in next-generation low-power superconducting electronics and quantum devices. Here, we design a family of 2D metal borocarbide superconductors with the chemical formula XB_6C_6 (X = Al, Ga, In) using a high-throughput structural search combined with first-principles calculations. These compounds crystallize in a graphene-like metal-intercalated structure, belonging to the layer group with $P\bar{6}2m$ symmetry, where metal atoms are intercalated between the honeycomb boron–carbon (B–C) layers. These compounds have an extremely low metal content, with 83% less metal than MgB_2 on a per-light-atom basis. The calculated results indicate that superconducting transition temperatures (T_c) of 2D InB_6C_6, GaB_6C_6, and AlB_6C_6 are 43.61 K, 42.20 K, and 39.97 K, respectively, all of which exceed the T_c values of the conventional MgB_2 superconductor (39 K). The high-T_c values of these 2D metal borocarbide superconductors are mainly attributed to the strong coupling between the metallized σ/π orbitals and the in-plane phonon vibrations of the B–C frameworks. These findings confirm that moderate metal doping in 2D light-element frameworks constitutes an effective strategy for achieving high-temperature superconductivity, thereby offering insights for the exploration of further superconductors.

DOI: 10.1103/yxtg-dcfj

I. INTRODUCTION

Since the discovery of superconductivity in 1911, the search for materials with increasingly higher critical temperatures has remained a central challenge in materials science and condensed matter physics [1–5]. Over the past few decades, superconductivity studies were mostly guided by the Bardeen–Cooper–Schrieffer (BCS) theory [6], which provides a fundamental microscopic framework for understanding conventional superconductivity mediated by electron–phonon coupling (EPC). In 2001, the discovery of MgB_2 with a T_c of 39 K at atmospheric pressure [7,8] reignited significant interest in the study of related light-element superconductors. The superconductivity of MgB_2 originates mainly from the strong coupling between metallicized σ electrons and the in-plane phonon modes within the boron layers [9]. According to the BCS theory, light elements tend to exhibit higher phonon frequencies, which favor elevated superconductivity. Boron and carbon are prototypical light elements capable of forming strong covalent bonds. Consequently, compounds based on the boron–carbon frameworks hold great potential to form strong covalent bonds or antibonding states near the Fermi level. These states can interact strongly with phonons, thereby forming robust EPC interactions and superconductivity [10–16]. At the same time, strong chemical bonds are also conducive to structural stability, a critical prerequisite for technological applications.

Recently, boron–carbon compounds have become a focus in high-temperature superconductor research, particularly metal-intercalated layered compounds, which have attracted considerable attention [17–23]. As early as 2002, Rosner *et al.* predicted a hole-doped Li_xBC ($x = 0.5$) to exhibit a T_c as high as 100 K [24]. However, creating metal vacancies to achieve hole doping often leads to lattice distortions, which may alter electronic band structure and phonon spectra, disrupting electron–phonon interactions and ultimately suppressing superconductivity [25]. Thus, the search for stable boron–carbon superconductors with a low metal content, based on the concept of minimizing metal vacancies, has long been a key objective in the field of light-element superconductors. Pham *et al.* reported the high-temperature superconductor MgB_3C_3, in which the number of Mg atoms is reduced by approximately 67% compared to the MgB_2 structure. EPC calculations show that the highest T_c of MgB_3C_3 could reach 59 K just by reducing the Mg concentration [26]. This T_c value is obviously higher than that of MgB_2. The electronic bands of MgB_3C_3 near the Fermi level are dominated by B and C

*Contact author: scu_kuang@163.com

†Contact author: a.hermann@ed.ac.uk

‡Contact author: lucheng@calypso.cn

 ©2026 American Physical Society

atoms, with two σ bonds and two π bonds contributing mainly to the total density of states (TDOS) around the Fermi level [26]. The layered nature of B–C compounds enables their exfoliation into two-dimensional (2D) geometries [23,27–31]. Modak *et al.* discovered that the chemical bonds of the B–C honeycomb layers change from sp^2 to sp^3 hybridization, when the bulk LiBC is exfoliated into a monolayer, causing 2D LiBC to become metallic [32]. The LiBC monolayer is predicted to exhibit superconductivity with a T_c of $\sim$ 70 K, which can be further enhanced by hydrogenation [32].

In 2020, Gao *et al.* verified a stable three-layer structure of LiB_2C_2 [23]. The electronic structure calculations revealed significant σ and π bonding character near the Fermi level. The phonon modes associated with bond stretching (E_u and E_g) exhibited strong coupling with the σ electrons. The 2D LiB_2C_2 structure is predicted to be a two-gap superconductor with a T_c of $\sim$92 K at ambient pressure. Moreover, the superconductivity of 2D LiB_2C_2 reaches 125 K by applying the biaxial tensile strain [23]. Subsequently, in 2022, S. Singh *et al.* found that the 2D $Mg_2B_4C_2$ achieves T_c values of 47–48 K without external regulations such as strain, doping, or substrate induction. The high-T_c value arises from the strong EPC and the high density of states (DOS) at the Fermi level [33]. By replacing the pure boron layer on the surface of the MgB_2 double-layer with B–C layers, the surface of the structure became inert and easier to synthesize [33]. Prior studies [22–28] have confirmed that the superconductivity in 2D ternary metal–boron–carbon compounds is dominated by the boron–carbon covalent frameworks, which serve as the major contributors to the total EPC interactions. Thus, the compounds with lower metal contents and a higher proportion of B–C honeycomb layers may lead to new discoveries in 2D superconductors with high superconductivity. In fact, boron doping is a direct method to enhance superconductivity, which often introduces lattice distortions that destabilize the layered geometry [34]. Metal doping can compensate for the charge deficiency of boron, thereby forming stable B–C compounds with balanced charge distributions [35]. In this work, we have identified a family of 2D superconductors, XB_6C_6 (X = Al, Ga, In), using the 2D CALYPSO structural search method and first-principles calculations. Its metal content is extremely low, with one metal atom for every 12 light atoms—a reduction of approximately 83% compared to MgB_2, which has one metal atom for every two light-element atoms. The XB_6C_6 superconductors contain single metal layers, which are intercalated between two B–C honeycomb layers. The calculated T_c values are 43.61 K for InB_6C_6, 42.20 K for GaB_6C_6, and 39.97 K for AlB_6C_6, all of which exceed the T_c of MgB_2 (39 K). The electronic states near the Fermi level are dominated by B and C atoms, with σ bonds from B–C hybridizations contributing the strong EPC interactions. Our results demonstrate that superconductivity in XB_6C_6 is primarily mediated by the coupling between metallized σ/π bonds and the in-plane phonons of the B–C covalent frameworks.

II. COMPUTATIONAL METHODS

The structural searches of 2D XB_6C_6 (X = Al, Ga, In) were performed using the CALYPSO [36–39] method and first-principles calculations. The stoichiometric ratio was fixed at 1:6:6 with 1–4 formula units per cell. A 20-Å vacuum layer was introduced to eliminate interlayer interactions between adjacent 2D slabs. Structure relaxations and electronic structure calculations were carried out using the Vienna *Ab initio* Simulation Package (VASP) [40–44]. The Perdew–Burke–Ernzerhof (PBE) functional within the generalized gradient approximation (GGA) was adopted, with a plane-wave cutoff energy of 600 eV. The DFT-D3 method was employed to account for the van der Waals (vdW) dispersion interactions in the layered structures. Convergence criteria were set to 1×10^{-8} eV for total energy and 1×10^{-5} eV/Å for force. Thermal stability was evaluated using *ab initio* molecular dynamics (AIMD) simulations in the NVT ensemble. A $2 \times 2 \times 1$ supercell was employed, and simulations were performed at 300 K, 500 K, and 1000 K for a total duration of 6 ps with a time step of 1 fs. Mechanical stability was assessed by calculating the elastic constants using the stress–strain method [45,46]. Dynamical stability was confirmed by phonon dispersion curves, which were calculated using the Phonopy code [46] based on density functional perturbation theory (DFPT) with a $2 \times 2 \times 1$ supercell. Crystal orbital Hamilton population (COHP) analysis was performed using the LOBSTER package [47]. EPC interactions and superconducting properties were computed by Quantum ESPRESSO [48,49]. Ultrasoft pseudopotentials were used to model the electron–ion interactions. The 2D Coulomb cutoff was enabled and a vacuum layer of 20 Å was included. The electronic occupations were treated using the Methfessel–Paxton smearing scheme. The kinetic energy cutoffs for wave functions and charge density were set to be 100 and 800 Ry, respectively. Convergence tests were performed for the k- and q-points, as shown in Fig. S1 within the Supplemental Material [50]. Dynamical matrices and EPC parameters were calculated using a $48 \times 48 \times 1$ k-point grid and a $12 \times 12 \times 1$ q-point mesh, with a degauss of 0.015 used for the final calculation. The T_c value was evaluated from the McMillan equation [51] as given by

$$T_c = \frac{\omega_{\log}}{1.2} \exp\left[\frac{-1.04(1+\lambda)}{\lambda - \mu^*(1+0.62\lambda)}\right], \tag{1}$$

where μ^* denotes the Coulomb pseudopotential. In this work, we adopted the typical value $\mu^* = 0.1$ [22], and compared the results with $\mu^* = 0.05$ and $\mu^* = 0.13$ [26]. The quantity $\omega_{\log}$ is the logarithmic average of phonon frequencies, and its expression is

$$\omega_{\log} = \exp\left[\frac{2}{\lambda}\int_0^\infty \frac{\alpha^2 F(\omega)}{\omega} \ln \omega d\omega\right]. \tag{2}$$

III. RESULTS AND DISCUSSION

To explore structures and superconducting properties of the 2D XB_6C_6 family, we adopted a simple calculation workflow, as illustrated in Fig. 1. First, an unbiased structural search is conducted using the 2D crystal structure prediction method based on the CALYPSO algorithm. Within the Al–B–C system, we successfully identified a stable trilayer configuration with a B:C ratio of 6:6. This stable AlB_6C_6 structure belongs to the $P\bar{6}2m$ symmetry. Subsequently, we expanded the search

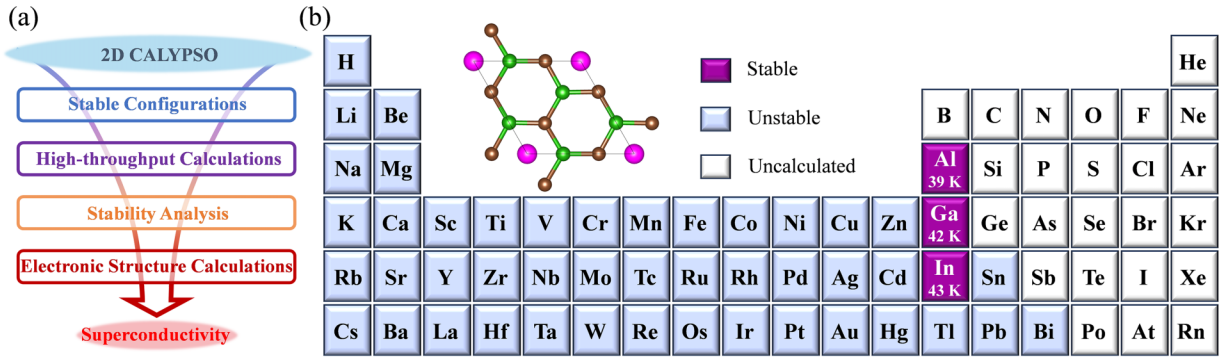


FIG. 1. (a) Computational workflow for 2D XB_6C_6 design and property prediction. (b) Periodic table of XB_6C_6 compounds. Pink and blue areas indicate dynamically stable and unstable structures, respectively, and white areas represent unexplored structures.

scope through high-throughput crystal structure calculations for a total of 48 potential XB_6C_6 candidate materials, as shown in Fig. 1(b). Comprehensive structural optimizations, rigorous stability analyses (including both dynamical and thermodynamic stabilities), and electronic property calculations were performed for these XB_6C_6 candidates. We discuss these aspects in detail in the following sections. As shown in Fig. 1(b), the pink shaded regions denote dynamically stable candidates with superconducting properties, whereas blue shaded regions represent unstable structures. Among the metallic elements and hydrogen in the periodic table, three stable structures were identified for group III elements. Thus, we mainly focus on these three dynamically stable structures, namely XB_6C_6 (X = Al, Ga, In).

For simplicity, Fig. 2(a) just shows the crystal structure of 2D InB_6C_6. The 2D structure exhibits a sandwich-like configuration, where a single layer of regularly arranged In atoms is intercalated between two adjacent B–C hexagonal honeycomb layers. The In atoms are situated at the central mirror plane of the 2D slab. The top and bottom B–C layers are symmetrically displaced along the vertical direction. The in-plane bond length distributions show two types of B–C covalent bonds, with bond lengths of $d_1 = 1.56$; Å and $d_2 = 1.55$ Å. Both values are obviously shorter than the B–B bond length of 1.77 Å in MgB_2. The shorter bond lengths lead to stronger orbital overlap between B and C atoms, facilitating the formation of strong covalent bonds (e.g., σ and π bonds), which promote phonon vibrations and enhance EPC strengths. Furthermore, these inequivalent B–C bonds provide more degrees of freedom for phonon vibrations in the lattice [26]. The interlayer spacing between the two B–C layers is about 3.84–3.91 Å, which exceeds the corresponding interlayer spacings in related compounds: 3.55 Å in $Li_3B_4C_2$ [17], 3.73 Å in MgB_3C_3 [26], 3.62 Å in Li_2BC_3 [30], 3.5 Å in $Mg_2B_4C_2$ [33], and 3.53 Å in MgB_2 [7]. This larger interlayer spacing may stem from the reduced concentration of intercalated metal atoms, which weakens interlayer binding and allows the B–C sheets to separate further, but could also result from the larger metal atom size.

To further verify the bonding characteristics and structural stability of InB_6C_6, we calculated the electron localization function (ELF), performed Bader charge analysis, and calculated the crystal orbital Hamiltonian population (COHP). First, the ELF results of InB_6C_6 are shown in Fig. 2(c). As shown in Fig. 2(c), electrons are clearly concentrated around the C atoms in 2D InB_6C_6. To quantify electron localization, we presented the electron concentration between B and C atoms in the (001) plane in Fig. 2(d). The ELF value in this region exceeds 0.95, confirming the strong covalent bonding between B and C atoms, which is consistent with the bond length results. We then calculated the Bader charges of

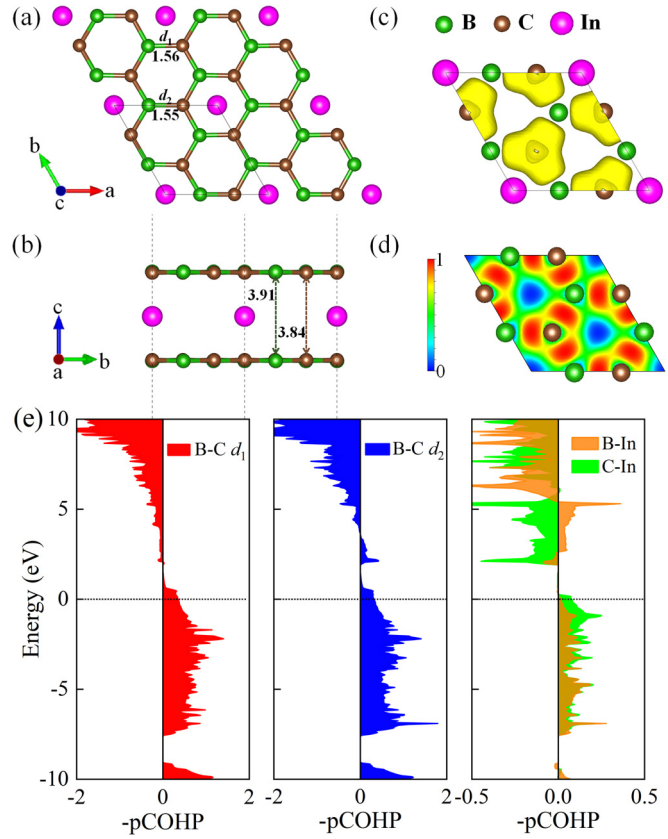


FIG. 2. (a) Top view of the 2D InB_6C_6 and the B–C bond lengths (Å). (b) Side view of the 2D InB_6C_6 and the spacing between the B–C layers (Å). (c) An electron localization function (ELF) isosurface with a value of 0.59, and (d) a 2D contour plot of the ELF in the (001) plane. (e) Negatively projected crystal orbital Hamiltonian populations (−pCOHP) of the B–C, In–B, and In–C bonds of 2D InB_6C_6.

TABLE I. Calculated lattice constants, B–C bond lengths (Å), and negative integrals COHP (-ICOHP, in eV/atom pair) values of XB_6C_6 (X = Al, Ga, In).

Compound	a (Å)	B–C d_1 (Å)	–ICOHP	B–C d_2 (Å)	–ICOHP	M–B (Å)	–ICOHP	M–C (Å)	–ICOHP
InB_6C_6	4.689	1.566	8.03	1.559	7.86	2.516	1.65	2.469	1.60
GaB_6C_6	4.681	1.562	7.96	1.560	7.79	2.337	1.98	2.280	2.10
AlB_6C_6	4.674	1.562	8.03	1.554	7.87	2.284	1.65	2.206	2.10

InB_6C_6 to quantify the charge transfer between In, B, and C atoms. The calculated results show that the In atom donates 1.22 e to the B–C layers within the unit cell. This charge transfer indicates ionic interactions between the intercalated metal atoms and the B–C layers, which promote the formation of the stable three-layer InB_6C_6. For isostructural AlB_6C_6 and GaB_6C_6, the Al and Ga atoms donate 1.94 e and 1.00 e, respectively. Metallic interlayer interactions may also play a crucial role in the structural stability of 2D InB_6C_6. The detailed Bader charges and charge transfer values of XB_6C_6 are listed in Table SI within the Supplemental Material [50].

The negative projection of COHP (−pCOHP) of InB_6C_6 is shown in Fig. 2(e). All bonds in InB_6C_6 exhibit positive values near the Fermi level, and no antibonding states appear at or near the Fermi level. This bonding characteristic contributes to the structural stability of InB_6C_6. Subsequently, we used the overlap integral method to analyze the contribution of each orbital to the overall bonding. The integrated COHP (−ICOHP) values are calculated for all interatomic bonds. The calculated results are summarized in Table I. We find that the two inequivalent B–C bonds with different bond lengths exhibit large −ICOHP values, which are 8.03 eV/atom pair and 8.75 eV/atom pair. The two B–C bond lengths are similar, resulting in comparable bond strengths. In contrast, the −ICOHP values of B–In and C–In are 1.65 eV/atom pair and 1.60 eV/atom pair, respectively, which are much smaller than those of the B–C bonds. These findings are consistent with our judgment of the interactions between B–C covalent bonds and In–B/C ionic bonds in the InB_6C_6. In addition, we also conducted a detailed analysis of AlB_6C_6 and GaB_6C_6, and present the lattice constants, B–C bond lengths, and −ICOHP values in Table I.

To assess the appropriateness of the vacuum thickness adopted for 2D InB_6C_6 and the structural robustness of its layer configuration, we separately tested the variation of energy with the thickness of the vacuum layer and the distance between the three atomic layers, as shown in Fig. S2 within the Supplemental Material [50]. First, we calculated the total energy as a function of the out-of-plane lattice parameter c, as shown in Fig. S2(a). The total energy gradually converges for $c \sim 20$ Å, confirming that the chosen vacuum thickness is sufficient to eliminate significant interactions between periodic images. Upon progressively reducing the vacuum thickness, we found a minimum in the total energy at $c = 7.8$ Å. This behavior suggests that, at sufficiently small c, interactions may develop between layers of adjacent periodic images along the z direction, potentially indicating a tendency toward the corresponding three-dimensional (3D) bulk structure. However, the associated energy difference is only 3.95 meV/Å^2, indicating that InB_6C_6 exhibits only a weak tendency to stack along the c direction. We subsequently performed full structural relaxation and phonon calculations for the $c = 7.8$ Å configuration. The calculated phonon spectrum for the $2 \times 2 \times 4$ supercell is shown in Fig. S3 within the Supplemental Material [50]. Although a faint imaginary frequency appears near the Γ point, we attribute it to an extremely low-frequency, very soft interlayer sliding mode leading to a Fourier interpolation artifact, rather than to an intrinsic structural instability. We consider this 3D InB_6C_6 structure to be dynamically stable and believe it may warrant further investigation in future work. The corresponding POSCAR file is provided in the Supplemental Material [50].

To further verify the robustness of the 2D sandwich-like configuration, we evaluated the interlayer binding between the B–C atomic layers and the central In layer. As shown in Fig. S2(b), the calculated binding energy (E_b) as a function of the displacement (d) indicates that an energy of up to 104.04 meV/Å^2 is required to separate InB_6C_6 into individual layers, demonstrating the presence of a pronounced potential well. This strong internal binding is fully consistent with the results of the ELF and COHP analyses, further confirming that the interaction between the In atoms and the B–C framework is not merely a weak van der Waals interaction but instead has a strong ionic-bonding character. Interestingly, we also observe an intermediate energy plateau in the range $d = 0.7$–1.2 Å before the system reaches its final equilibrium energy. To examine whether this feature is robust with respect to the treatment of van der Waals interactions, we compared calculations based on PBE, DFT-D3 with zero damping, and DFT-D3 with Becke–Johnson damping. All three approaches consistently exhibit a transient energy plateau, as shown in Fig. S4 within the Supplemental Material [50]. These calculations also show the binding energy of our compound to be quite insensitive to the functional. We further calculated the Bader charges to elucidate the evolution of the electronic structure during the separation process in Fig. S5 within the Supplemental Material [50]. The Bader analysis shows that, over an intermediate separation range of approximately 0.8–1.3 Å, the charge state of In changes from +1.22 at equilibrium to +0.57, indicating a distinct quasistable charge region. The observed energy plateau may therefore originate from a relatively stable intermediate electronic configuration. Given that In can exhibit not only its most stable (+3) oxidation state but also the (+1) oxidation state, we speculate that this plateau may be associated with an In^{+1}-like electronic configuration. It should also be noted that no structural relaxation was performed for any of the single-point energy calculations; consequently, residual internal stresses may remain in the structures and could contribute to the observed behavior. Overall, 2D InB_6C_6 exhibits a combination of weak interlayer coupling and strong intralayer cohesion. This distinctive bonding characteristic not only contributes to the

structural integrity of the framework but also ensures a high degree of out-of-plane stability for the isolated monolayer configuration.

To verify the mechanical, dynamical, and thermal stability of $X\mathrm{B_6C_6}$, we performed comprehensive stability assessments by calculating elastic constants, phonon dispersion curves, and *ab initio* molecular dynamics (AIMD) simulations, respectively. First, we calculated the elastic constants using the stress–strain method [45,46]. The calculation results are listed in Table SII within the Supplemental Material [50]. All mechanical stability criteria are satisfied, confirming that $X\mathrm{B_6C_6}$ are mechanically stable. Then, the phonon dispersion curves of $X\mathrm{B_6C_6}$ show no imaginary-frequency modes in the entire Brillouin zone, suggesting their dynamical stability. For a freestanding two-dimensional sheet, the out-of-plane acoustic (ZA) branch is expected to exhibit a quadratic dispersion near Γ. An enlarged view of the phonon dispersion near Γ is provided in the Supplemental Material (Fig. S6) [50]. We next examined the thermodynamic stability of $X\mathrm{B_6C_6}$ via AIMD simulations. All simulations were carried out in the canonical (NVT) ensemble with a time step of 2 fs and a total simulation duration of 10 ps. Stabilities were explored at three representative temperatures, i.e., 300 K, 500 K, and 1000 K. The simulated results are presented in Fig. S7 within the Supplemental Material [50].

The total energy of $\mathrm{InB_6C_6}$ fluctuates slightly around the average value, without any abrupt variations. As the temperature is increased to 1000 K, the total energies increase noticeably, and the temperature fluctuations become more pronounced. Structural snapshots of $\mathrm{InB_6C_6}$ after 10 ps of simulation are also displayed in Fig. S7 within the Supplemental Material [50]. At room temperature (300 K) and moderately high temperature (500 K), the crystal geometry is well preserved, and the three-layered sandwich-like configuration remains intact, with no signs of structural collapse or instability. These observations confirm the high thermal stability of $\mathrm{InB_6C_6}$ at 300 K and 500 K. Even at 1000 K, the $\mathrm{InB_6C_6}$ still maintains its three-layer atomic geometry. The hexagonal frameworks of the B–C layers remain intact, but the metal In atoms become detached from the B–C layers, causing the shifts in the three layers and a partial disruption of the long-range crystalline order. This phenomenon is best interpreted as a thermally induced structural rearrangement rather than framework decomposition. Such high-temperature structural distortion in $\mathrm{InB_6C_6}$ is consistent with that of the previously reported similar three-layered 2D material $\mathrm{KB_6C_6}$ [22]. In summary, the structure exhibits thermal stability under normal operating conditions. However, extremely high temperatures may trigger structural rearrangement, thereby limiting its stability in high-temperature applications. Following the discussions of the dynamical, thermal, and mechanical stability, we further evaluated the thermodynamic stability of the system by calculating its formation energy according to $E_f = \frac{E(\mathrm{InB_6C_6}) - E(\mathrm{In}) - 6E(\mathrm{B}) - 6E(\mathrm{C})}{13}$. Here, the reference energies of In, B, and C were taken from bulk In, bulk B, and graphite, respectively. The calculated formation energy of $\mathrm{InB_6C_6}$ is 0.31 eV/atom. The positive formation energy indicates that the system is thermodynamically unfavorable relative to the chosen elemental reference states and may therefore represent a metastable phase rather than the thermodynamic ground state. Similar behavior has also been reported for some previously proposed two-dimensional materials [52,53]. Whether such a two-dimensional structure can be experimentally synthesized remains to be verified.

To gain further insight into the electronic properties of the $X\mathrm{B_6C_6}$ family, we analyzed the electronic band structure, projected density of states (PDOS), and Fermi surface of $\mathrm{InB_6C_6}$, as shown in Fig. 3. Both the electronic band structure and TDOS indicate that $\mathrm{InB_6C_6}$ is a metal, with multiple energy bands crossing the Fermi level and a high density of states near the Fermi level. As shown in Fig. 3(a), the σ- and π-bonding states arising from B–C interactions contribute substantially to the density of states near the Fermi level, with the intercalated In atoms playing a negligible role (denoted in red, blue, and green, respectively). The presence of strong covalent σ and π bonds at the Fermi level is similar to the electronic properties of many reported superconducting materials. Specifically, the hybridized σ bonds dominate the DOS at the Fermi level, which is consistent with the electronic properties of H-$\mathrm{MgB_2}$ [29], $\mathrm{SrB_3C_3}$ [34], and $\mathrm{LiB_2C_2}$ [23] superconductors. The DOS at the Fermi level of $\mathrm{InB_6C_6}$ is as high as 3.885 states/eV per unit cell. A large DOS at the Fermi energy is the key electronic feature of light-element-based high-temperature superconductors, as demonstrated in numerous studies [22–28]. The large DOS at the Fermi level of $\mathrm{InB_6C_6}$ implies that more electrons participate in low-energy phonon scattering, which facilitates the formation of Cooper pairs, thereby enhancing the effective EPC interactions and elevating the superconducting critical temperature.

Notably, a distinct flat band appears near the Fermi level in the band structure at the M point [highlighted by the pink circle in Fig. 3(a)], located at ∼0.42 eV above the Fermi level, corresponding to a PDOS peak of 4.91 states/eV per unit cell. The coexistence of flat bands and DOS peaks is a signature of Van Hove singularity (VHS). Previous studies have shown that bands with VHS at the Fermi level favor the formation of high-T_c EPC-mediated superconductors. This phenomenon has been verified in various superconductors [12,13,34,54,55]. Here, $\mathrm{InB_6C_6}$ exhibits one VHS near the Fermi level, making it a highly promising EPC superconductor.

The Fermi surfaces of $\mathrm{InB_6C_6}$ with orbital projections are shown in Figs. 3(b)–3(d). The Fermi surfaces of $\mathrm{InB_6C_6}$ consist of eight independent pockets centered at the Γ point and include three concentric circles, four quasihexagonal shapes, and small arcs at the outermost edge. The innermost first and second Fermi surfaces are formed by a combination of σ bonds, π bonds, and In-d bonds. The third to sixth Fermi sheets are dominated by strong B–C σ bonds, with a maximum value of 0.76, which exceeds 0.4 in the $\mathrm{KB_2C_2}$ [27]. Zhang *et al.* reported that the superconductivity of $\mathrm{KB_2C_2}$ originates from strong coupling between σ bonds and interlayer covalent bond stretching modes [27]. The seventh and eighth Fermi sheets are dominated by B–C π bonds. While the contribution of In-d orbitals is relatively small, it is most prominent in the outermost arc-shaped pockets, where the hybridization of B–C π and In-d orbitals forms six small μ sheets. The Fermi surface of $\mathrm{InB_6C_6}$ exhibits hole-type pockets around the Γ point, which is similar to the known graphene-like layered $\mathrm{KB_2C_2}$ superconductor [22].

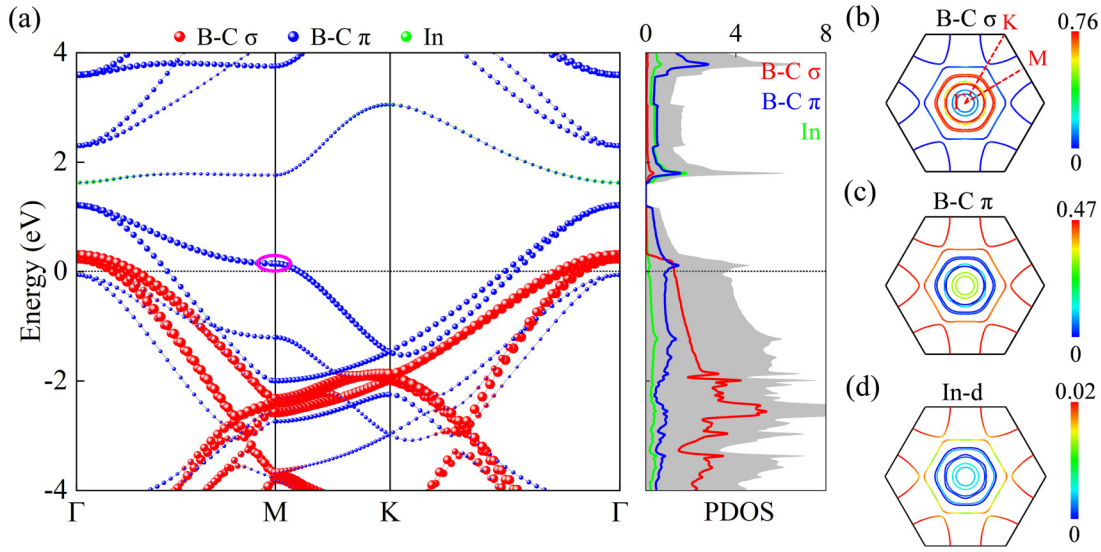


FIG. 3. (a) Electronic band structure and PDOS of InB_6C_6. The pink circle indicates the VHS. (b)–(d) Distribution of B–C σ, π, and *In-d* orbitals on the Fermi surface. High-symmetry paths and points are shown in red.

Moreover, we also calculated the band structure and DOS of AlB_6C_6 and GaB_6C_6, as shown in Fig. S8 within the Supplemental Material [50]. AlB_6C_6 and GaB_6C_6 exhibit electronic properties similar to InB_6C_6. There are six energy bands crossing the Fermi level. As illustrated in Fig. S8, the σ bonds and π bonds formed by B–C interactions contribute significantly near the Fermi level, whereas the contributions from the intercalated Al and Ga atoms are weak. The hybridized B–C σ bonds dominate the DOS near the Fermi level, but their strengths are slightly lower than those of InB_6C_6. The comparison results are summarized in Table II. Furthermore, we also found a typical VHS near the Fermi level at the M point in both AlB_6C_6 and GaB_6C_6. These electronic properties are consistent with those of InB_6C_6 and support the expectation that the entire XB_6C_6 family exhibits superconducting properties. Previous studies have demonstrated that the proximity of VHS to Fermi level favors a high superconducting critical temperature T_c [12,13,34]. Given this, we infer that InB_6C_6 may exhibit a higher-T_c value than AlB_6C_6 and GaB_6C_6.

The superconducting critical temperatures were calculated using the McMillan equation. The EPC constant λ of InB_6C_6 is 1.35, and the calculated T_c value of InB_6C_6 is 43.61 K. Similarly, the λ values for AlB_6C_6 and GaB_6C_6 are 1.07 and 1.26, respectively, yielding T_c values of 39.97 K for AlB_6C_6 and 42.20 K for GaB_6C_6. A summary of simulated parameters is listed in Table II. The T_c of the traditional metal-intercalated MgB_2 superconductor is 39 K. Notably, the T_c values of 2D XB_6C_6 all exceed this value, highlighting that metal-intercalated boron–carbon frameworks represent promising candidates for high-T_c superconductors. Although the McMillan formula directly depends on the semiempirical Coulomb repulsion parameter μ^*, the calculated results are widely accepted in the field of conventional superconductors. In this work, we adopted the commonly used value of $\mu^* = 0.1$, and compared the results for $\mu^* = 0.05$ and 0.13 [26] to assess the sensitivity of T_c to this parameter. The calculated results were also summarized in Table II.

To find the underlying superconducting mechanism of XB_6C_6, we calculated the phonon spectra weighted by electron–phonon coupling constants, the projected phonon density of states (PhDOS), the Eliashberg spectral function $\alpha^2F(\omega)$, and the electron–phonon coupling integral $\lambda(\omega)$. The calculation results of InB_6C_6 are presented in Fig. 4. The phonon dispersion spectra span the frequency range of 0 to 40 THz. As shown in Fig. 4(a), the PhDOS reveals that In atoms make a substantial contribution to the low-frequency region of the phonon spectra. A prominent peak is observed at 2.15 THz, with a smaller secondary peak at 8.06 THz, corresponding to PhDOS values of 9.14 states/THz and 0.84 states/THz, respectively. The mid-frequency and high-frequency regions of the phonon spectra are dominated by the vibrations of the B and C atoms, with nearly identical fluctuations in their projected phonon density of states. The

TABLE II. Calculated superconducting parameters of XB_6C_6, including the TDOS at the Fermi level [states/eV/cell], the DOS of the σ electrons at the Fermi level [states/eV/cell], the logarithmic frequency average, the EPC constant, and the superconducting transition temperature T_c for different values of μ^*.

Compound	$N(E_F)$	$N(E_F)_\sigma$	$\omega_{\log}$	λ	$T_c^{\mu^*=0.05}$ (K)	$T_c^{\mu^*=0.13}$ (K)	$T_c^{\mu^*=0.1}$ (K)
InB_6C_6	3.885	1.42	425.301	1.350	50.81	39.30	43.61
GaB_6C_6	3.272	1.24	445.695	1.257	49.80	37.68	42.20
AlB_6C_6	3.014	1.20	517.359	1.073	48.82	34.79	39.97

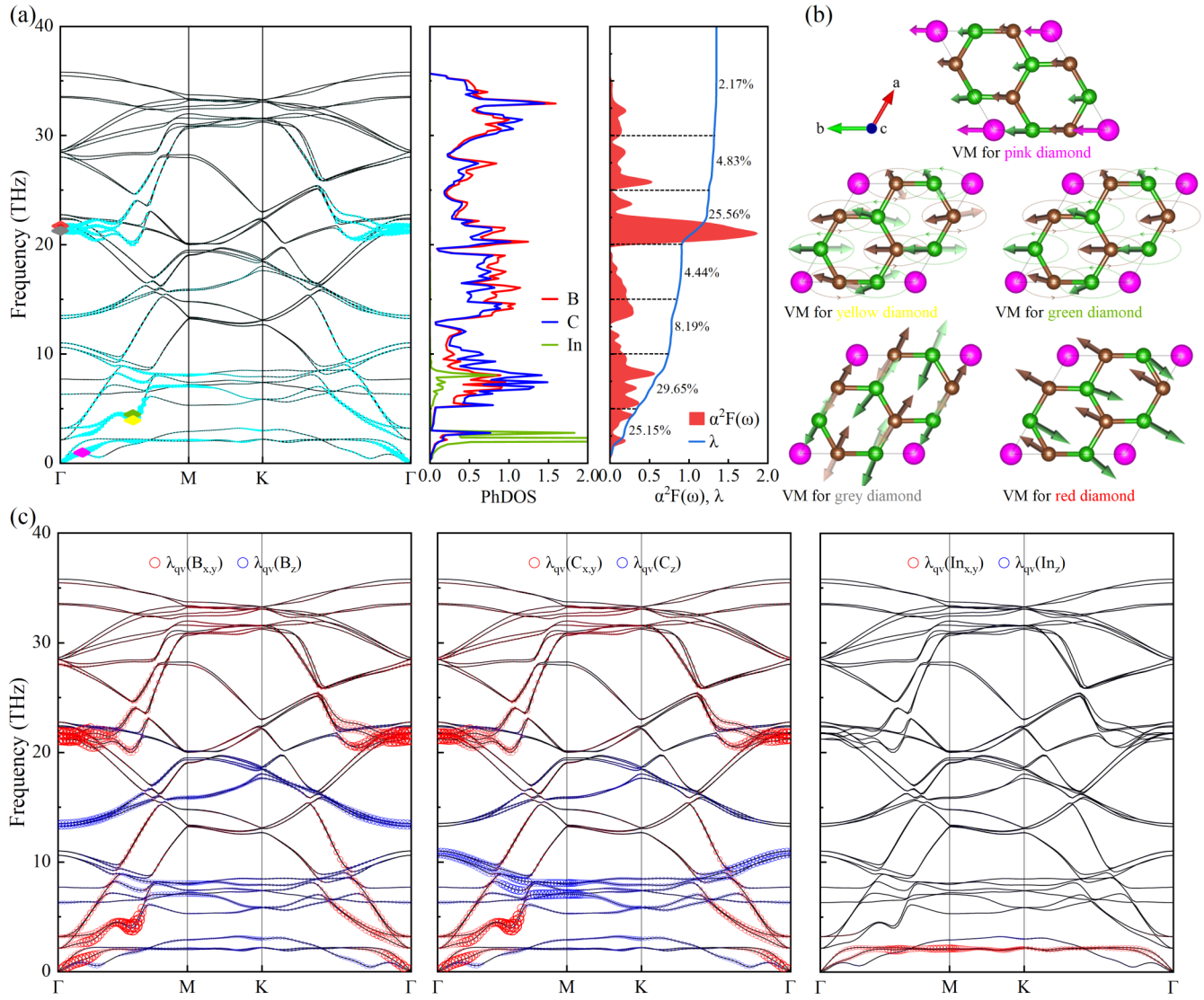


FIG. 4. (a) Calculated phonon dispersion curves of InB_6C_6 weighted by the mode-resolved phonon linewidths (cyan circles), together with the phonon density of states (PhDOS), Eliashberg spectral function $\alpha^2F(\omega)$, and EPC parameter $\lambda(\omega)$. The five diamonds in the phonon spectra indicate the five selected vibrational modes whose atomic displacement patterns are shown in (b). (c) Decomposition of the EPC parameter λ_{qv} into B/C/In-derived vibrational contributions, resolved into in-plane (xy) and out-of-plane (z) components.

covalent interactions arising from B–C hybridization may be the origin of strong EPC in InB_6C_6.

To gain deeper insight into the EPC in InB_6C_6, we calculated the phonon spectrum weighted by the phonon linewidths, as indicated by the cyan circles in Fig. 4(a), which are predominantly concentrated in the low- and intermediate-frequency regions. We therefore selected five representative vibrational modes for detailed analysis. The top views of the atomic displacement patterns of these five modes along the c axis are shown in Fig. 4(b). All atoms undergo in-plane vibrations within the xy plane. The pink arrows denote the displacements of the In atoms, while the green and brown arrows represent the motions of the B and C atoms, respectively. Where the displacement directions of the two B–C layers differ, the atomic displacements in the lower B–C layer are indicated by semitransparent arrows. The corresponding mode indices, λ_{qv}, ω_{qv}, and q points for the five selected modes are summarized in Table SIII within the Supplemental Material [50]. The pink diamond region in Fig. 4(a) corresponds to an acoustic phonon mode along the $\Gamma - M$ path. As illustrated in Fig. 4(b), the In atoms vibrate in the xy plane predominantly along the b axis, while the B and C atoms undergo vibrations in the same direction with comparatively smaller amplitudes. The yellow and green diamond markers in Fig. 4(a) occur at the same q point and both exhibit pronounced phonon softening. Their corresponding displacement patterns are shown in Fig. 4(b). In both modes, the B–C layers are deformed by rotations of the B_3C_3 rings within the xy plane, whereas the In atoms remain nearly stationary. All three of these representative modes lie in the low-frequency region. In the intermediate-frequency region of the phonon spectrum, we identify two strongly coupled phonon modes at the Γ point, marked by gray and red diamonds, respectively. Both modes are doubly degenerate and exhibit pronounced phonon softening. As shown in Fig. 4(b), while the In atoms remain nearly stationary, these modes induce

distortions of the B_3C_3 six-membered rings, with the B and C atoms within the same plane moving in opposite directions. This behavior is consistent with the phonon characteristics reported for the trilayer LiB_2C_2 superconductor, in which the in-plane vibrations of B and C atoms couple strongly to the electronic states and mediate the superconducting pairing [23].

To further elucidate the relationship between the EPC and the directions of atomic vibrations, we projected the λ_{qv} onto individual atoms and xy-z directions, as shown in Fig. 4(c). Consistent with the analysis of the representative vibrational modes discussed above, the in-plane vibrations of the B and C atoms within the xy plane provide the dominant contribution to the EPC. Notably, all five representative modes analyzed in Fig. 4(b) fall within the region of enhanced EPC contributions highlighted by the red circles in Fig. 4(c). In addition, the z-direction vibrations of B and C atoms contribute appreciably to λ in the low- and intermediate-frequency regions. In contrast, the metallic In atoms contribute to the EPC predominantly through their in-plane vibrations at low frequencies, consistent with the vibrational pattern of the mode marked by the pink diamond in Fig. 4(a). Overall, the EPC of InB_6C_6 is dominated by phonons involving in-plane vibrations of In, B, and C atoms, with the B–C framework making the most substantial contribution.

The EPC interactions in InB_6C_6 were further quantified using the Eliashberg spectral function $\alpha^2F(\omega)$. The EPC constants $\lambda(\omega)$ obtained through integration are shown in Fig. 4(a), with the percentage contributions indicating the increases in $\lambda(\omega)$ within the corresponding frequency intervals. In the low-frequency region of 0–10 THz, $\lambda(\omega)$ rises rapidly and steadily, accounting for more than half of the total EPC strength. In particular, the 5–10 THz range gives the largest contribution to $\lambda(\omega)$, accounting for 29.65% of the total value. The In atoms and the in-plane vibrations of the B and C atoms, corresponding to the pink, yellow, and green diamond-marked modes, are primarily responsible for this rapid increase in $\lambda(\omega)$. In the subsequent 10–20 THz region, the increase in $\lambda(\omega)$ is comparatively moderate and is mainly associated with the z-direction vibrations of the B and C atoms, possibly reflecting the weaker EPC associated with out-of-plane atomic motion compared with the dominant in-plane modes. In the intermediate-frequency range of 20–30 THz, the $\alpha^2F(\omega)$ reaches its largest peak in the 20–23 THz interval. This feature corresponds to the two doubly degenerate softened modes marked by the gray and red diamonds in Fig. 4(a), which give rise to another pronounced increase in the integrated EPC constant. These results indicate that the electronic states near the Fermi level couple strongly to phonons primarily associated with the in-plane vibrations of the B–C framework in InB_6C_6. The strong B–C hybridization and the resulting robust covalent σ bonds provide an important microscopic origin for this strong EPC. Moreover, the electronic states associated with the splitting of these bonding states contribute to the formation of steep electronic bands near the Fermi level, a feature that can favor strong electron–phonon coupling and thus facilitate superconductivity [56]. For comparison, we also calculated the phonon spectrum weighted by the phonon linewidths, projected phonon density of states, Eliashberg spectral functions $\alpha^2F(\omega)$, and integrated EPC constants $\lambda(\omega)$ for AlB_6C_6 and GaB_6C_6, as shown in Fig. S9 within the Supplemental Material [50].

Given the substantial contribution of low-frequency phonons to the electron–phonon coupling, we note that approximately 25% of the total electron–phonon coupling constant $\lambda(\omega)$ comes from the low-frequency range of 0–5 THz. We therefore further examined the validity of the harmonic approximation for InB_6C_6. Using the frozen phonon approach, we performed potential energy surface scans along selected phonon eigenvectors, with the results presented in the Supplemental Material (Figs. S10–S12 within the Supplemental Material [50]). Specifically, we selected Mode 4 and Mode 5 at the Γ point and Mode 2 at the M point, and systematically varied the modulation amplitude Q along the corresponding phonon eigenvectors. Single-point energy calculations were performed for each mode over the range of $Q = -2 \ldots + 8$. The atomic structures at $Q = 0$ and $Q = 8$ are also shown in the Supplemental Material [Figs. S10–S12(c)] to illustrate the corresponding atomic displacements along the selected eigenvector directions. For all three modes, $E(Q)$ reaches its minimum at $Q = 0$ and exhibits an approximately parabolic dependence on Q. Moreover, the energy profiles for positive and negative Q are nearly symmetric, indicating that odd-order terms make only a negligible contribution within the investigated range. We therefore fitted the calculated energy profiles using both a purely quadratic form, $\Delta E = c_2Q^2$, and a form including the leading fourth-order anharmonic correction, $\Delta E = c_2Q^2 + c_4Q^4$. The fitting results are summarized in Figs. S10–S12(b). For all three modes, the quadratic fits alone yield $R^2 > 0.999$, while inclusion of the fourth-order term results in only a marginal improvement in the fitting quality. As shown in Figs. S10–S12(a), the DFT data points, the quadratic fits, and the quartic-corrected fits are nearly indistinguishable over the entire range of Q. These results indicate that, for the selected phonon modes and displacement range, the corresponding potential energy surfaces are predominantly governed by the quadratic term, with only minor contributions from fourth-order anharmonicity. In particular, no pronounced anharmonic behavior is observed for the low-frequency modes examined here despite their substantial contribution to the EPC. These results support the applicability of the harmonic approximation to the phonon and EPC calculations for InB_6C_6 within the investigated range, thereby providing additional confidence in the calculated value of $\lambda(\omega)$.

In principle, the metal elements in the XB_6C_6 all belong to group IIIA of the periodic table, which lies at the boundary between metals and nonmetals, with three valence electrons in their outermost shell. Changing the intercalated metal directly modulates the interlayer spacing of the hexagonal B–C layers and the number of energy states involved in superconductivity, which in turn influences the lattice vibrations and EPC interactions. Compared with the previously reported $X^{3+}[B_3C_3]^{3-}$ compounds [57], the addition of Al, Ga, and In atoms in the $[B_6C_6]^{3-}$ frameworks forms hole-doped metals. The band structures of undoped bilayer $[B_6C_6]$ compounds (where metal atoms are removed from the calculations) exhibit rigid-band behavior [11], as shown in Fig. S13 within the Supplemental Material: the removal of intercalants has a negligible effect on the shape of the electronic bands,

but shifts the positions of the Fermi levels. The calculated phonon spectrum of the B–C bilayer indicates dynamical instability, whereas the introduction of the intercalated metal atoms donates electrons to form ionic bonds with the B–C layers, thereby stabilizing the three-layer geometries of XB_6C_6.

Among the XB_6C_6 family, InB_6C_6 exhibits the largest DOS at the Fermi level, reaching 3.885 states/eV/cell, while the values for GaB_6C_6 (3.27 states/eV/cell) and AlB_6C_6 (3.01 states/eV/cell) are lower, as shown in Table II. This confirms the strong correlation between the DOS at the Fermi level and the superconducting transition temperature T_c. Meanwhile, the metallized σ bonds are known to play a pivotal role in high-temperature superconductivity [22]. We summarized the DOS contributions from hybridized B–C σ bonds at the Fermi level, as shown in Table II, which are 1.42 states/eV/cell for InB_6C_6, 1.24 states/eV/cell for GaB_6C_6, and 1.20 states/eV/cell for AlB_6C_6, and are consistent with the increasing order of T_c values for XB_6C_6 compounds. Thus, the coupling between metallized σ bonds and in-plane phonon vibrations of the B–C layers is one of the primary origins of superconductivity in 2D XB_6C_6, which is analogous to the superconducting mechanism of MgB_2 [7].

In fact, the π bonds also make a significant contribution to superconductivity in XB_6C_6. In the electronic band structures of XB_6C_6, VHSs are formed by π bonds. The corresponding DOS values are 4.91 states/eV/cell for InB_6C_6, 3.06 states/eV/cell for GaB_6C_6, and 2.72 states/eV/cell for AlB_6C_6. The magnitudes of the DOS at the VHSs are correlated with the superconducting transition temperatures. Among them, InB_6C_6 exhibits the highest T_c value of 43.61 K. This result confirms that flat bands near the Fermi level facilitate the superconductivity of borides and carbides [57,58]. Thus, we can deduce that the metallized σ and π bonds that couple with the in-plane phonons of the B–C layers are the main drivers of superconductivity in XB_6C_6. Our results verify that 2D XB_6C_6 are structurally stable and possess excellent superconductivity. Their T_c values are comparable to the 39 K of the MgB_2 superconductor. A high density of states at the Fermi level, strong σ and π bonds, flat bands, and VHSs are potential descriptors for the identification of high-T_c metal–light-element superconductors.

Finally, compared with previously reported two-dimensional borocarbides, the predicted T_c of XB_6C_6, approximately 40–43 K, is not among the highest, despite their lowest metal content. In fact, while reducing the metal content can modify the electronic structure near the Fermi level and the charge transfer between the metal and B/C atoms, the T_c is governed by multiple intertwined factors, including the electronic structure, $\lambda(\omega)$, and $\omega_{\log}$. Importantly, in InB_6C_6, In does not merely serve as a charge-regulating center. The In-related low-frequency modes also make a significant contribution to the EPC. These modes can enhance the EPC strength while simultaneously lowering $\omega_{\log}$, resulting in competing effects on T_c. Thus, reducing the metal content does not completely eliminate the contribution of the metal atoms to the superconducting pairing mechanism. Consequently, although XB_6C_6 possesses a high fraction of B–C covalent bonding and an exceptionally low metal content, its relatively low $\omega_{\log}$, together with the substantial contribution of In-related low-frequency phonons to the EPC, limits further enhancement of T_c. Therefore, the structural and chemical characteristics associated with reduced metal content do not automatically translate into a higher T_c. Instead, the metal content, electronic structure, phonon spectrum, and electron–phonon coupling are interconnected through a complex interplay rather than a simple monotonic relationship.

IV. CONCLUSIONS

In summary, through high-throughput density functional theory (DFT) calculations, we have predicted a family of 2D intercalated boron–carbon superconductors of XB_6C_6 (X = Al, Ga, In). The stable XB_6C_6 (X = Al, Ga, In) adopt a graphite-like intercalated structure with the layer group $P\bar{6}2m$, where metal atoms are intercalated between two hexagonal B–C honeycomb layers. These compounds have an extremely low metal content. The T_c values of InB_6C_6, GaB_6C_6, and AlB_6C_6 are 43.61 K, 42.20 K, and 39.97 K, respectively, all exceeding the T_c of MgB_2 (39 K). The outstanding superconductivities are attributed to the strong coupling between metallized σ/π bonds and the in-plane phonon vibrations of the B–C covalent frameworks in XB_6C_6. These findings highlight that appropriate metal doping into strongly covalent frameworks is an effective strategy for achieving high-T_c superconductivity in 2D metal–light-element superconductors, which offers a new pathway for research into low-dimensional superconducting materials.

ACKNOWLEDGMENTS

This work was supported by the National Key Research and Development Program of China (Grant No. 2025YFA1411002), the National Natural Science Foundation of China (Grant No. 12174352), the Guangdong Basic and Applied Basic Research Foundation (Grant No. 2026A1515011030), and the Joint Fund of Henan Province Science and Technology R&D Program (Grant No. 245200810086).

DATA AVAILABILITY

There are no publicly available research data or software supporting this manuscript. Requests for further information or data should be sent to the authors.

[1] S. A. Li, R. Niu, Y. M. Liu, X. Fu, X. J. Chen, H. Q. Lin, and G. H. Zhong, Ambient-pressure high-temperature superconductivity exceeding 100 K in three-dimensional carbon structures, Phys. Rev. B **111**, 054523 (2025).

[2] J. M. Lu, O. Zheliuk, I. Leermakers, N. F. Q. Yuan, U. Zeitler, K. T. Law, and J. T. Ye, Evidence for two-dimensional Ising superconductivity in gated MoS_2, Science **350**, 1353 (2015).

[3] E. K. Ko, Y. Yu, Y. Liu, L. Bhatt, J. Li, V. Thampy, C.-T. Kuo, B. Y. Wang, Y. Lee, K. Lee, *et al.*, Signatures of ambient pressure superconductivity in thin film $La_3Ni_2O_7$, Nature (London) **638**, 935 (2025).

[4] H. Sun, M. Huo, X. Hu, J. Li, Z. Liu, Y. Han, L. Tang, Z. Mao, P. Yang, B. Wang, *et al.*, Signatures of superconductivity near 80 K in a nickelate under high pressure, Nature (London) **621**, 493 (2023).

[5] Z. Guo, A. Bergara, X. Zhang, X. Li, S. Ding, and G. Yang, Superconductivity in Li_8H_n electrides: The effect of interstitial anionic electrons on electron-phonon coupling, Phys. Rev. B **109**, 134505 (2024).

[6] J. Bardeen, L. N. Cooper, and J. R. Schrieffer, Theory of superconductivity, Phys. Rev. **108**, 1175 (1957).

[7] J. Nagamatsu, N. Nakagawa, T. Muranaka, Y. Zenitani, and J. Akimitsu, Superconductivity at 39 K in magnesium diboride, Nature (London) **410**, 63 (2001).

[8] J. Kortus, I. I. Mazin, K. D. Belashchenko, V. P. Antropov, and L. L. Boyer, Superconductivity of metallic boron in MgB_2, Phys. Rev. Lett. **86**, 4656 (2001).

[9] S. Tajima, T. Masui, J. Quilty, S. Lee, A. Yamamoto, and A. Yamanaka, Experimental study of electron-phonon interaction in MgB_2, Physica C **388-389**, 103 (2003).

[10] T. E. Weller, M. E. Ellerby, S. S. Saxena, R. P. Smith, and N. T. Skipper, Superconductivity in the intercalated graphite compounds C_6Yb and C_6Ca, Nat. Phys. **1**, 39 (2005).

[11] J. Li, J. Yue, S. Guo, A. Zhang, L. Zhu, H. Song, Z. Liu, Y. Liu, and T. Cui, High-temperature superconductivity of boron-carbon clathrates at ambient pressure, Phys. Rev. B **109**, 144509 (2024).

[12] S. Lu, H. Liu, I. I. Naumov, S. Meng, Y. Li, J. S. Tse, B. Yang, and R. J. Hemley, Superconductivity in dense carbon-based materials, Phys. Rev. B **93**, 104509 (2016).

[13] Y. Zhao, X. Nie, S. Zeng, S. Wang, G. Li, Z. Dai, Y. Yin, C. Lian, and J. Ni, Superconductivity in hexagonal BC monolayer-based films, Phys. Rev. B **111**, 174524 (2025).

[14] T. T. Gai, P. J. Guo, H. C. Yang, Y. Gao, M. Gao, and Z. Y. Lu, Van Hove singularity induced phonon-mediated superconductivity above 77 K in hole-doped SrB_3C_3, Phys. Rev. B **105**, 224514 (2022).

[15] P. Zhang, X. Li, X. Yang, H. Wang, Y. Yao, and H. Liu, Path to high-T_c superconductivity via Rb substitution of guest metal atoms in the SrB_3C_3 clathrate, Phys. Rev. B **105**, 094503 (2022).

[16] Y. L. Han, K. Y. Jiang, B. T. Wang, P. Zhang, and H. Y. Lu, Anisotropic high-T_c superconductivity above 90 K in hole-doped boron-nitrogen clathrates at ambient pressure, Phys. Rev. B **111**, 094520 (2025).

[17] M. Gao, Z. Y. Lu, and T. Xiang, Prediction of phonon-mediated high-temperature superconductivity in $Li_3B_4C_2$, Phys. Rev. B **91**, 045132 (2015).

[18] M. Gao, X. W. Yan, Z. Y. Lu, and T. Xiang, Phonon-mediated high-temperature superconductivity in the ternary borohydride KB_2H_8 under pressure near 12 GPa, Phys. Rev. B **104**, L100504 (2021).

[19] Y. Quan and W. E. Pickett, $Li_{2x}BC_3$: Prediction of a second MgB_2-class high-temperature superconductor, Phys. Rev. B **102**, 144504 (2020).

[20] F. Zheng, Y. Sun, R. Wang, Y. Fang, F. Zhang, S. Wu, C. Z. Wang, V. Antropov, and K. M. Ho, Superconductivity in the Li-B-C system at 100 GPa, Phys. Rev. B **107**, 014508 (2023).

[21] C. Zhang, H. Tang, C. Pan, H. Jiang, H. J. Sun, K. M. Ho, and C. Z. Wang, Machine learning guided discovery of superconducting calcium borocarbides, Phys. Rev. B **108**, 024512 (2023).

[22] H. D. Liu, X. P. Fu, Z. G. Fu, H. Lu, and P. Zhang, High-T_c and three-gap two-dimensional superconductors with electronic and phononic topology: KB_2C_2, Phys. Rev. B **111**, 184502 (2025).

[23] M. Gao, X. W. Yan, Z. Y. Lu, and T. Xiang, Strong-coupling superconductivity in LiB_2C_2 trilayer films, Phys. Rev. B **101**, 094501 (2020).

[24] H. Rosner, A. Kitaigorodsky, and W. E. Pickett, Prediction of high T_c superconductivity in hole-doped LiBC, Phys. Rev. Lett. **88**, 127001 (2002).

[25] A. M. Fogg, P. R. Chalker, J. B. Claridge, G. R. Darling, and M. J. Rosseinsky, LiBC electronic, vibrational, structural, and low-temperature chemical behavior of a layered material isoelectronic with MgB_2, Phys. Rev. B **67**, 245106 (2003).

[26] T. T. Pham and D. L. Nguyen, First-principles prediction of superconductivity in MgB_3C_3, Phys. Rev. B **107**, 134502 (2023).

[27] Y. Zhang, J. Chen, J. Hao, M. Xu, and Y. Li, Conventional high-temperature superconductivity in σ-band driven metallized two-dimensional metal borocarbides, Phys. Rev. B **110**, 064513 (2024).

[28] H. D. Liu, B. T. Wang, Z. G. Fu, H. Y. Lu, and P. Zhang, Three-gap superconductivity with T_c above 80 K in hydrogenated 2D monolayer LiBC, Phys. Rev. Res. **6**, 033241 (2024).

[29] J. Bekaert, M. Petrov, A. Aperis, P. M. Oppeneer, and M. V. Milošević, Hydrogen-induced high-temperature superconductivity in two-dimensional materials: The example of hydrogenated monolayer MgB_2, Phys. Rev. Lett. **123**, 077001 (2019).

[30] T. Bazhirov, Y. Sakai, S. Saito, and M. L. Cohen, Electron-phonon coupling and superconductivity in Li-intercalated layered borocarbide compounds, Phys. Rev. B **89**, 045136 (2014).

[31] J. Bekaert, A. Aperis, B. Partoens, P. M. Oppeneer, and M. V. Milošević, Evolution of multigap superconductivity in the atomically thin limit: Strain-enhanced three-gap superconductivity in monolayer MgB_2, Phys. Rev. B **96**, 094510 (2017).

[32] P. Modak, A. K. Verma, and A. K. Mishra, Prediction of superconductivity at 70 K in a pristine monolayer of LiBC, Phys. Rev. B **104**, 054504 (2021).

[33] S. Singh, A. H. Romero, J. D. Mella, V. Eremeev, E. Muñoz, A. N. Alexandrova, K. M. Rabe, D. Vanderbilt, and F. Muñoz, High-temperature phonon-mediated superconductivity in monolayer $Mg_2B_4C_2$, npj Quantum Mater. **7**, 37 (2022).

[34] J. N. Wang, X. W. Yan, and M. Gao, High-temperature superconductivity in SrB_3C_3 and BaB_3C_3 predicted from first-principles anisotropic Migdal-Eliashberg theory, Phys. Rev. B **103**, 144515 (2021).

[35] Q. Jiang, Z. Huo, Z. Liu, L. Chen, T. Ma, S. Jiang, D. Duan, and T. Cui, Modulation of superconductivity and superhardness in XB_4C_4 (X = Be, B, Al, Si, P, and Ti) borocarbides at ambient pressure, Phys. Rev. B **111**, 224515 (2025).

[36] Y. Wang, J. Lv, L. Zhu, and Y. Ma, CALYPSO: A method for crystal structure prediction, Comput. Phys. Commun. **183**, 2063 (2012).

[37] Y. Wang, J. Lv, L. Zhu, and Y. Ma, Crystal structure prediction via particle-swarm optimization, Phys. Rev. B **82**, 094116 (2010).

[38] H. Wang, Y. Wang, J. Lv, Q. Li, L. Zhang, and Y. Ma, CALYPSO structure prediction method and its wide application, Comput. Mater. Sci. **112**, 406 (2016).

[39] B. Gao, P. Gao, S. Lu, J. Lv, Y. Wang, and Y. Ma, Interface structure prediction via CALYPSO method, Sci. Bull. **64**, 301 (2019).

[40] G. Kresse and J. Furthmüller, Efficient iterative schemes for *ab initio* total-energy calculations using a plane-wave basis set, Phys. Rev. B **54**, 11169 (1996).

[41] J. Hafner, *Ab-initio* simulations of materials using VASP: Density-functional theory and beyond, J. Comput. Chem. **29**, 2044 (2008).

[42] V. Wang, N. Xu, J. C. Liu, G. Tang, and W. T. Geng, VASPKIT: A user-friendly interface facilitating high-throughput computing and analysis using VASP code, Comput. Phys. Commun. **267**, 108033 (2021).

[43] G. Kresse and J. Furthmüller, Efficiency of ab-initio total energy calculations for metals and semiconductors using a plane-wave basis set, Comput. Mater. Sci. **6**, 15 (1996).

[44] J. Hafner, Materials simulations using VASP—A quantum perspective to materials science, Comput. Phys. Commun. **177**, 6 (2007).

[45] S. Yalameha, Z. Nourbakhsh, and D. Vashaee, ElTools: A tool for analyzing anisotropic elastic properties of the 2D and 3D materials, Comput. Phys. Commun. **271**, 108195 (2022).

[46] V. Wang, G. Tang, Y. C. Liu, R. T. Wang, H. Mizuseki, Y. Kawazoe, J. Nara, and W. T. Geng, High-throughput computational screening of two-dimensional semiconductors, J. Phys. Chem. Lett. **13**, 11581 (2022).

[47] S. Maintz, V. L. Deringer, A. L. Tchougréeff, and R. Dronskowski, LOBSTER: A tool to extract chemical bonding from plane-wave based DFT, J. Comput. Chem. **37**, 1030 (2016).

[48] P. Giannozzi, S. Baroni, N. Bonini, M. Calandra, R. Car, C. Cavazzoni, D. Ceresoli, G. L. Chiarotti, M. Cococcioni, I. Dabo, *et al.*, QUANTUM ESPRESSO: A modular and open-source software project for quantum simulations of materials, J. Phys.: Condens. Matter **21**, 395502 (2009).

[49] P. Giannozzi, O. Andreussi, T. Brumme, O. Bunau, M. B. Nardelli, M. Calandra, R. Car, C. Cavazzoni, D. Ceresoli, M. Cococcioni, *et al.*, Advanced capabilities for materials modelling with QUANTUM ESPRESSO, J. Phys.: Condens. Matter **29**, 465901 (2017).

[50] See Supplemental Material at http://link.aps.org/supplemental/10.1103/yxtg-dcfj for additional structural and stability analyses, Bader charge analyses, phonon dispersions, electronic properties, and frozen-phonon calculations, as well as structural files for InB_6C_6..

[51] P. B. Allen and R. C. Dynes, Transition temperature of strong-coupled superconductors reanalyzed, Phys. Rev. B **12**, 905 (1975).

[52] S. Ono and H. Satomi, High-throughput computational search for two-dimensional binary compounds: Energetic stability versus synthesizability of three-dimensional counterparts, Phys. Rev. B **103**, L121403 (2021).

[53] D. Wines, K. Choudhary, A. J. Biacchi, K. F. Garrity, and F. Tavazza, High-throughput DFT-based discovery of next generation two-dimensional (2D) superconductors, Nano Lett. **23**, 969 (2023).

[54] L. Van Hove, The occurrence of singularities in the elastic frequency distribution of a crystal, Phys. Rev. **89**, 1189 (1953).

[55] Y. Liu, Y. Zhang, M. Xu, J. Feng, J. Hao, and Y. Li, Van Hove singularity, flat bands, Dirac states, and superconductivity in van der Waals–bonded and covalently bonded bilayer borophene with a coloring triangular lattice, Phys. Rev. B **111**, 085401 (2025).

[56] C. Chen, J. Miao, J. Zuo, S. He, and C. Lu, Superconductivity of metal doped-boron-nitrogen clathrates under ambient pressure, Phys. Rev. B **110**, 174514 (2024).

[57] N. Geng, K. P. Hilleke, L. Zhu, X. Wang, T. A. Strobel, and E. Zurek, Conventional high-temperature superconductivity in metallic, covalently bonded, binary-guest C–B clathrates, J. Am. Chem. Soc. **145**, 1696 (2023).

[58] Y. Cao, V. Fatemi, S. Fang, K. Watanabe, T. Taniguchi, E. Kaxiras, and P. Jarillo-Herrero, Unconventional superconductivity in magic-angle graphene superlattices, Nature (London) **556**, 43 (2018).